

# A doubly-localized equilibrium solution of plane Couette flow

E. BRAND AND J. F. GIBSON

Dept. of Mathematics and Statistics, University of New Hampshire, Durham, NH 03824, USA

(Received 3 April 2014; Revised 1 May 2014; Accepted 3 May 2014)

We present an equilibrium solution of plane Couette flow that is exponentially localized in both the spanwise and streamwise directions. The solution is similar in size and structure to previously computed turbulent spots and localized, chaotically wandering edge states of plane Couette flow. A linear analysis of dominant terms in the Navier-Stokes equations shows how the exponential decay rate and the wall-normal overhang profile of the streamwise tails are governed by the Reynolds number and the dominant spanwise wavenumber. Perturbations of the solution along its leading eigenfunctions cause rapid disruption of the interior roll-streak structure and formation of a turbulent spot, whose growth or decay depends on the Reynolds number and the choice of perturbation.

## 1. Introduction

Since the work of Nagata (1990) a large number of unstable nonlinear equilibrium, traveling-wave, and periodic-orbit solutions of the Navier-Stokes equations have been computed for a variety of canonical flows including pipe, channel, plane Couette, and square-duct flow. These invariant solutions demonstrate the feasibility and fruitfulness of treating well-resolved direct numerical simulations as very-high-dimensional dynamical systems, and they capture, in a precise and elemental form, a number of important coherent flow structures and dynamical processes. Linear stability analysis shows that these solutions have relatively few unstable modes, and that the solutions and their low-dimensional unstable manifolds impose structure on the dynamics of moderately turbulent flows. See Kawahara *et al.* (2012) for a recent review of this work. Most of this work has been done in the context of canonical flows in small computational domains with periodic boundary conditions, resulting in spatially periodic solutions that lie within dynamically invariant periodic subspaces of the same flows on infinite domains. While small periodic ‘minimal flow units’ are useful microcosms for studying turbulence, turbulence in extended domains generally involves large numbers of interacting flow structures, whose dynamic coupling presumably decreases with their separation. Additionally the transition to turbulence in extended domains occurs through the growth of turbulent spots or puffs, consisting of localized patches of unsteady, complex flow within a background of laminar flow (Wynanski & Champagne 1973; Tillmark & Alfredsson 1992; Barkley & Tuckerman 2005; Philip & Manneville 2011).

These considerations motivate the search for spatially-localized invariant solutions of flows in extended domains. Schneider *et al.* (2010*b*) found the first known localized solutions, a pair of spanwise-localized, streamwise-periodic equilibrium and traveling-wave solutions of plane Couette flow, further investigated in Schneider *et al.* (2010*a*). Avila *et al.* (2013) found a streamwise-localized relative periodic orbit of pipe flow that closely resembles the transient turbulent puffs of Hof *et al.* (2006). Deguchi *et al.* (2013) and Gibson & Brand (2014) independently found spanwise-localized forms of the periodic EQ7/HVS solution of Itano & Generalis (2009); Gibson *et al.* (2009). Gibson & Brand

(2014) also presented a number of spanwise-localized and wall-normal-localized traveling waves of channel flow. Khapko *et al.* (2013) found spanwise-localized relative periodic orbits of the asymptotic suction boundary layer, and Zammert & Eckhardt (2014) found a spanwise- and wall-normal-localized periodic orbit of plane Poiseuille flow.

This paper presents a span- and streamwise-localized equilibrium solution of plane Couette flow, the first known invariant solution of the Navier-Stokes equations localized in two homogeneous directions. The numerical procedure by which the doubly-localized solution was found is outlined in §2. Properties of the solution are presented in §3, including its exponential localization, its global quadrupolar flow, the geometrical structure of its rolls and streaks, its wall-normal overhang profile, and the role of its instabilities in the transition to turbulence.

## 2. Computation of doubly-localized solutions

The mathematical formulation and numerical methods are presented in detail in Gibson & Brand (2014) (GB14); here we present a brief outline. The Reynolds number  $Re$  for plane Couette flow is defined in terms of half the relative wall speed, the channel half-height, and the kinematic viscosity, so that the walls at  $y = \pm 1$  have velocity  $\pm 1$  and the laminar flow solution is given by  $y \mathbf{e}_x$ . The total velocity is expressed as a sum of the laminar flow and the deviation from laminar,  $\mathbf{u}_{\text{tot}} = y \mathbf{e}_x + \mathbf{u}$ , and henceforth we refer to the deviation  $\mathbf{u} = [u, v, w]$  as velocity. With these assumptions  $\mathbf{u}$  has zero Dirichlet boundary conditions at the walls, and the nondimensionalized Navier-Stokes equations take the form

$$\frac{\partial \mathbf{u}}{\partial t} + y \frac{\partial \mathbf{u}}{\partial x} + v \mathbf{e}_x + \mathbf{u} \cdot \nabla \mathbf{u} = -\nabla p + \frac{1}{Re} \nabla^2 \mathbf{u}, \quad \nabla \cdot \mathbf{u} = 0. \quad (2.1)$$

The nondimensionalized computational domain is  $[-L_x/2, L_x/2] \times [-1, 1] \times [-L_z/2, L_z/2]$  with periodic boundary conditions in the streamwise  $x$  and spanwise  $z$  directions. Discretization is performed with standard Fourier-Chebyshev spectral methods in space, 3rd-order semi-implicit finite differencing in time, and 2/3-style dealiasing. The computational domain and spatial discretization are specified in terms of  $L_x \times L_z$  and the collocation grid  $N_x \times N_y \times N_z$ . Equilibria are computed as solutions of  $\mathbf{f}^T(\mathbf{u}) - \mathbf{u} = 0$ , where  $\mathbf{f}^T$  is the time integration of (2.1) for a fixed time  $T$ , and the discretized equations are solved with a Newton-Krylov-hookstep search algorithm (Viswanath 2007, 2009). The choice for the  $T$  is determined by a practical balance in the computational solution of the Newton-step equation: too small a value of  $T$  results in weak viscous damping and slow convergence of the iterative GMRES algorithm, but too large  $T$  reduces the distance  $\|\delta \mathbf{u}\|$  over which the linearization  $f^T(\mathbf{u} + \delta \mathbf{u}) \approx f^T(\mathbf{u}) + Df^T \delta \mathbf{u}$  is accurate. We have found that  $T = O(10)$  is a good balance for a wide variety of flow conditions and Reynolds numbers. The software and the numerical data for the doubly-localized solution are available at [www.channelflow.org](http://www.channelflow.org) (Gibson *et al.* 2008; Gibson 2014).

Initial guesses for the doubly-localized solutions were produced by applying streamwise windowing to the spanwise-localized forms of EQ7 solution from GB14, or two-dimensional windowing to the doubly-periodic EQ7 solution from Gibson *et al.* (2009). We used the same tanh-based windowing function as in GB14 equation (2.4), replacing  $z$  with  $x$  for a streamwise windowing function

$$W(x) = \frac{1}{4} \left( 1 + \tanh \left( \frac{6(a-x)}{b} + 3 \right) \right) \left( 1 + \tanh \left( \frac{6(a+x)}{b} + 3 \right) \right). \quad (2.2)$$

As noted in GB14,  $W(x)$  is even, smooth, monotonic in  $|x|$ , and close to unity for the

core region  $|x| < a$ , transitions smoothly to nearly zero over  $a < |x| < a + b$ , and approaches zero exponentially as  $|x| \rightarrow \infty$ . The nonzero divergence of windowed velocity fields  $W(x)\mathbf{u}(x, y, z)$  is fixed by revising the wall-normal  $v$  component to satisfy incompressibility. To create doubly-localized initial guesses from doubly-periodic solutions, we applied the two-dimensional windowing function  $W(x)W(z)$  with different length scales for the core and transition regions in the streamwise and spanwise directions.

It was considerably more difficult to find doubly-localized solutions from windowed initial guesses than it was to find the spanwise-localized solutions of GB14. Not only do the doubly-localized solutions require doubly-extended domains, the decay rate of their tails is slower than for the spanwise-localized solutions (see § 3.3), and thus the computational domains must be larger in both  $x$  and  $z$ . Search results were sensitive both to the wavelengths of the underlying periodic or spanwise localized solution and to the choice of windowing parameters. The search landscape for doubly-localized solutions is also vastly more complicated and more sensitive to spatial discretization, with many nonzero local minima and many spurious solutions for under-resolved discretizations. Lastly, doubly-localized initial guesses tended to converge onto the trivial solution  $\mathbf{u} = 0$  (laminar flow), with the search quickly settling onto streaky flow with very little streamwise variation, and then reducing the magnitude of the streaks to zero. Such streaks are dynamical transients that decay to laminar flow under time evolution, but their decay is slow enough that they nearly satisfy the search equation  $\mathbf{f}^T(\mathbf{u}) - \mathbf{u} = 0$  for small  $T$ , thus attracting nearby guesses to a search path that ultimately leads to  $\mathbf{u} = 0$ .

To prevent the search algorithm from being fooled by such transients, we modified the search equation to  $(\mathbf{f}^T(\mathbf{u}) - \mathbf{u})/(\|\mathbf{u}\|_{3d} - c) = 0$ , where  $\|\mathbf{u}\|_{3d}$  is the energy norm (see § 3.4) of the streamwise-varying portion of  $\mathbf{u}$  and  $c$  is a parameter set to some fraction of the value of  $\|\mathbf{u}\|_{3d}$  for the initial guess. Our choices for underlying periodicity and windowing parameters were determined by trial and error, guided by the length scales that approximate solutions took on during the search. To mitigate computational costs, we performed trial-and-error calculations in relatively small domains with poor localization ( $80 \times 20$  and  $O(10^{-1})$  tails at the perimeter) and then extended solutions from successful searches to larger domains where localization is more pronounced ( $200 \times 200$  with  $O(10^{-3})$  tails), using either continuation in  $L_x, L_z$  or simply doubling the computational domain and reapplying windowing. For doubly-localized solutions we found that solutions were reliably robust to changes in discretization when spectral coefficients were retained to  $O(10^{-7})$  in  $x, z$  and  $O(10^{-10})$  in  $y$ . The solution presented in the following section is the most robust of several we found, in that it converges quickly at higher spatial resolutions and continues smoothly and easily in  $L_x, L_z$  and  $Re$ . This solution was found by applying two-dimensional windowing to the doubly-periodic EQ7 solution, refinement to an exact solution by Newton-Krylov-hookstep, and extension to large domains by repeated doubling, windowing, and refinement.

### 3. Properties of the doubly-localized solution

#### 3.1. Global flow

Figure 1 shows a doubly-localized equilibrium solution of plane Couette flow in a  $200 \times 120$  computational domain at  $Re = 240$ , discretized with  $720 \times 49 \times 1024$  gridpoints. The solution has the symmetry group  $\{e, \sigma_{xy}, \sigma_z, \sigma_{xyz}\}$  where

$$\begin{aligned} \sigma_{xy} : [u, v, w](x, y, z) &\rightarrow [-u, -v, w](-x, -y, z), \\ \sigma_z : [u, v, w](x, y, z) &\rightarrow [u, v, -w](x, y, -z), \end{aligned} \quad (3.1)$$

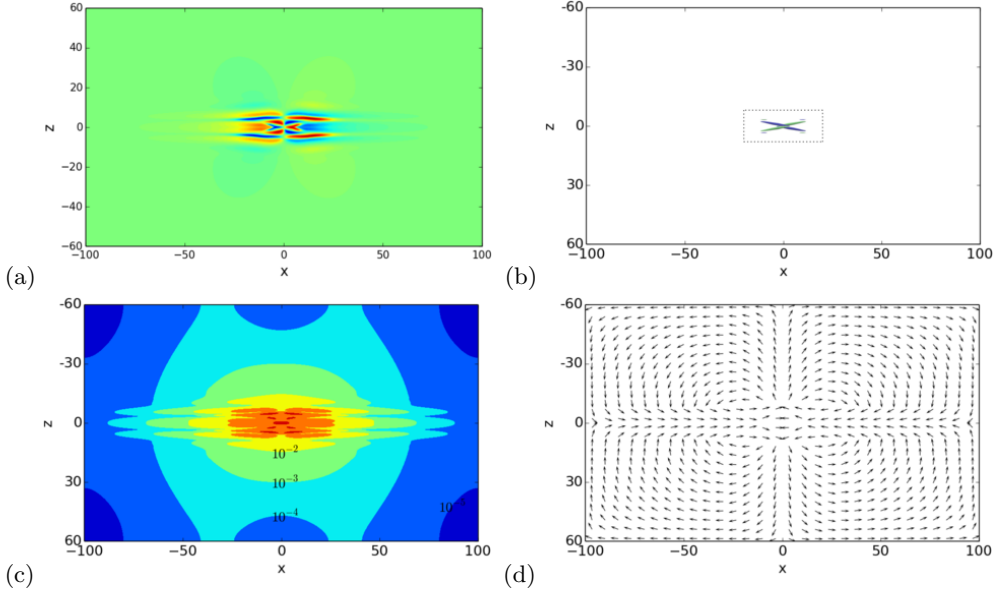


FIGURE 1. **A doubly-localized equilibrium solution of plane Couette flow at  $Re = 240$  in a  $200 \times 120$  computational domain.** (a) Streamwise velocity  $u$  in the  $y = 0$  midplane. The blue-red color axis spans  $u \in [-0.5, 0.5]$ . (b) Isosurfaces of swirling strength at  $s = \pm 0.2$  in green/blue, indicating swirling with clockwise/counterclockwise orientation with respect to the positive  $x$  axis. The dotted  $40 \times 16$  subdomain is shown in detail in figure 2. (c) Exponential localization, indicated by contours of  $y$ -integrated energy (see text). Contour levels are set at  $10^{-n}$  for  $n = 0, 1, \dots, 5$ ; the boundaries for  $10^{-2}$  through  $10^{-5}$  are labeled. (d) Quadrupolar  $y$ -averaged global flow, shown by a vector plot of  $(\bar{u}, \bar{w})/\sqrt{\bar{u}^2 + \bar{w}^2}$ , where  $\bar{u}, \bar{w}$  are the  $y$  averages of  $u, w$ . Note that the vector spacing in this plot is too coarse to resolve rapid variations in the region surrounding the origin.

$\sigma_{xyz} = \sigma_{xy}\sigma_z$  and  $e$  is the identity. We use standard angle-bracket notation from group theory to specify groups in terms of their generators, e.g.  $\langle \sigma_{xy}, \sigma_z \rangle = \{e, \sigma_{xy}, \sigma_z, \sigma_{xyz}\}$ . The doubly-localized solution acquires  $\langle \sigma_{xy}, \sigma_z \rangle$  symmetry from the windowing breaking the symmetries of EQ7 that involve  $x$  and  $z$  translation, in the same manner as EQ7-2 of GB14. The streamwise velocity in the  $y = 0$  midplane, shown in Figure 1(a), is roughly comparable to the dynamically wandering doubly-localized edge state at  $Re = 400$  shown in figure 5 of Schneider *et al.* (2010b). Both display patterns of wavy streaks that are spanwise narrow and streamwise elongated, and the significant non-laminar structure in both is confined to a roughly  $100 \times 20$  subdomain of the flow. Figure 1(c) shows that the solution is exponentially localized in both span- and streamwise directions, via contours of the  $y$ -integrated energy  $e(x, z) = 1/2 \int_{-1}^1 \mathbf{u} \cdot \mathbf{u} dy$ . The fingers that extend along the  $x$  axis are due to small-wavelength, exponentially decaying streaks of streamwise velocity (see §3.3). The deviation from elliptical contours near the edges of the computational domain is an artifact of the periodicity of the domain, which, together with the solution symmetries, induces even symmetry of  $e$  about  $x = \pm L_x/2$  and  $z = \pm L_z/2$ . In larger computational domains we have observed elliptical contours and exponential decay over four orders of magnitude, with comparable decay rates in  $x$  and  $z$ .

Figure 1(d) shows the direction of the  $y$ -averaged flow  $(\bar{u}, \bar{w})$  by a vector plot of  $(\bar{u}, \bar{w})/\sqrt{\bar{u}^2 + \bar{w}^2}$ . Note the quadrupolar character of the  $y$ -averaged flow, similar to figure 6 of Schumacher & Eckhardt (2001) and figure 3 of Duguet & Schlatter (2013). The  $\bar{u}, \bar{w}$  flow is streamwise inward along  $z = 0$  and spanwise outward along  $x = 0$ , with a global

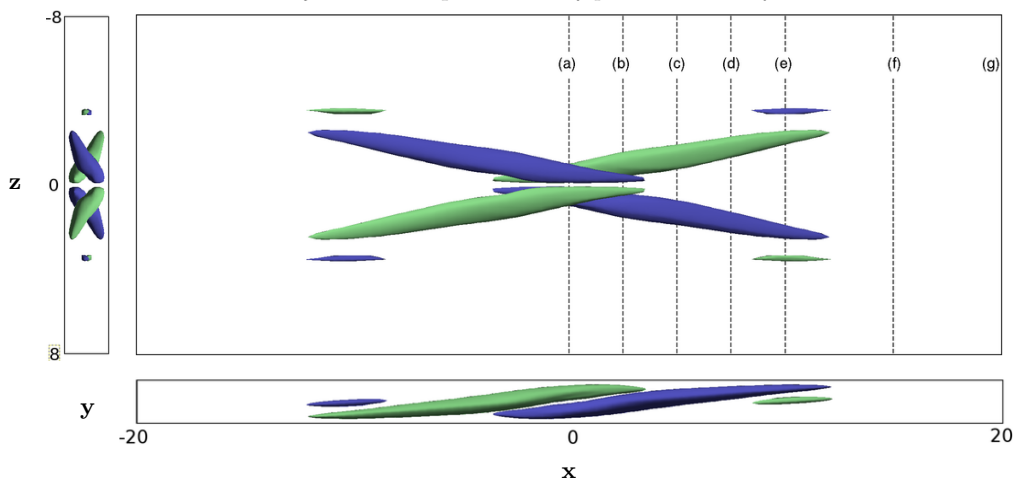


FIGURE 2. **Three-dimensional structure of swirling strength.** Isosurfaces of signed swirling strength at  $s = \pm 0.2$  in green/blue. The upper-right subfigure is a blow-up of the  $x \in [-20, 20]$ ,  $z \in [-8, 8]$  subdomain in figure 1(b). Dotted lines show the  $x$ -positions of the streamwise-normal cross sections depicted in figure 3, with (a)-(g) at  $x = \{0, 2.5, 5, 7.5, 10, 15, 20\}$ . Views of the same structure (left) in  $y, z$  and (bottom) in  $x, y$ .

circulation in each of the four quadrants. The alignment of the  $y$ -averaged flow with the  $x$  and  $z$  axes also results from symmetry:  $\sigma_z$  symmetry requires that  $u$  and  $w$  are even and odd in  $z$ , respectively, about  $z = 0$ , and  $\sigma_{xy}$  symmetry requires that  $\bar{u}$  and  $\bar{w}$  are odd and even in  $x$  about  $x = 0$ . Periodicity in  $x$  and  $z$  requires the same symmetries about the  $x = \pm L_x/2$  and  $z = \pm L_z/2$  edges of the computational domain, so that the  $y$ -averaged flow aligns with these edges as well (see Gibson *et al.* (2009)).

### 3.2. Internal structure

The localized patterns of high- and low-speed streaks shown in figure 1(a) are generated by the highly localized roll structure illustrated in figure 1(b). The latter shows isosurfaces of signed swirling strength at  $s = \pm 0.2$ , about 1/3 of its maximum value. Swirling strength is defined as the magnitude of the imaginary part of the complex eigenvalues of the velocity gradient tensor  $\nabla \mathbf{u}$  (Zhou *et al.* 1999). Signed swirling strength includes a  $\pm$  sign indicating the orientation of swirling (Wu & Christensen 2006), here the sign of the  $x$  component of the swirling axis when oriented with the right-hand-rule. The swirling is highly localized: the magnitude of swirling drops by a factor of roughly ten between the X-shaped isosurfaces and the edges of the dotted box that marks a  $40 \times 16$  subdomain. Figure 2 shows a detail of the swirling strength in this subdomain with the same plotting conventions as figure 1(b). The three perspective plots show an overall X-shaped structure composed of two overlapping  $\Lambda$ -shaped vortices, whose legs swirl in opposite directions and tilt in both the spanwise and wall-normal directions. Small, weaker vortices of opposite sign flank the legs near their ends.

Figure 3 further illustrates the three-dimensional structure of the  $\Lambda$ -shaped vortices and their relation to streamwise streaks. The flow in streamwise-normal cross-sections is shown at  $x$  positions indicated by lines marked (a-g) in figure 2. The  $x = 0$  plane in (a) shows the  $y$ -symmetric tips of the two opposed  $\Lambda$ -shaped vortices, concentrated near  $z = 0$ , each drawing midplane fluid towards the wall to form streaks. As  $x$  increases in (b)-(d), the swirling of the legs grows in strength, size, and spacing, and moves from the lower wall towards the upper. By (e) the legs have reached the upper wall and weakened, but the opposite-signed vortices that flank the tips of the legs have grown to their greatest

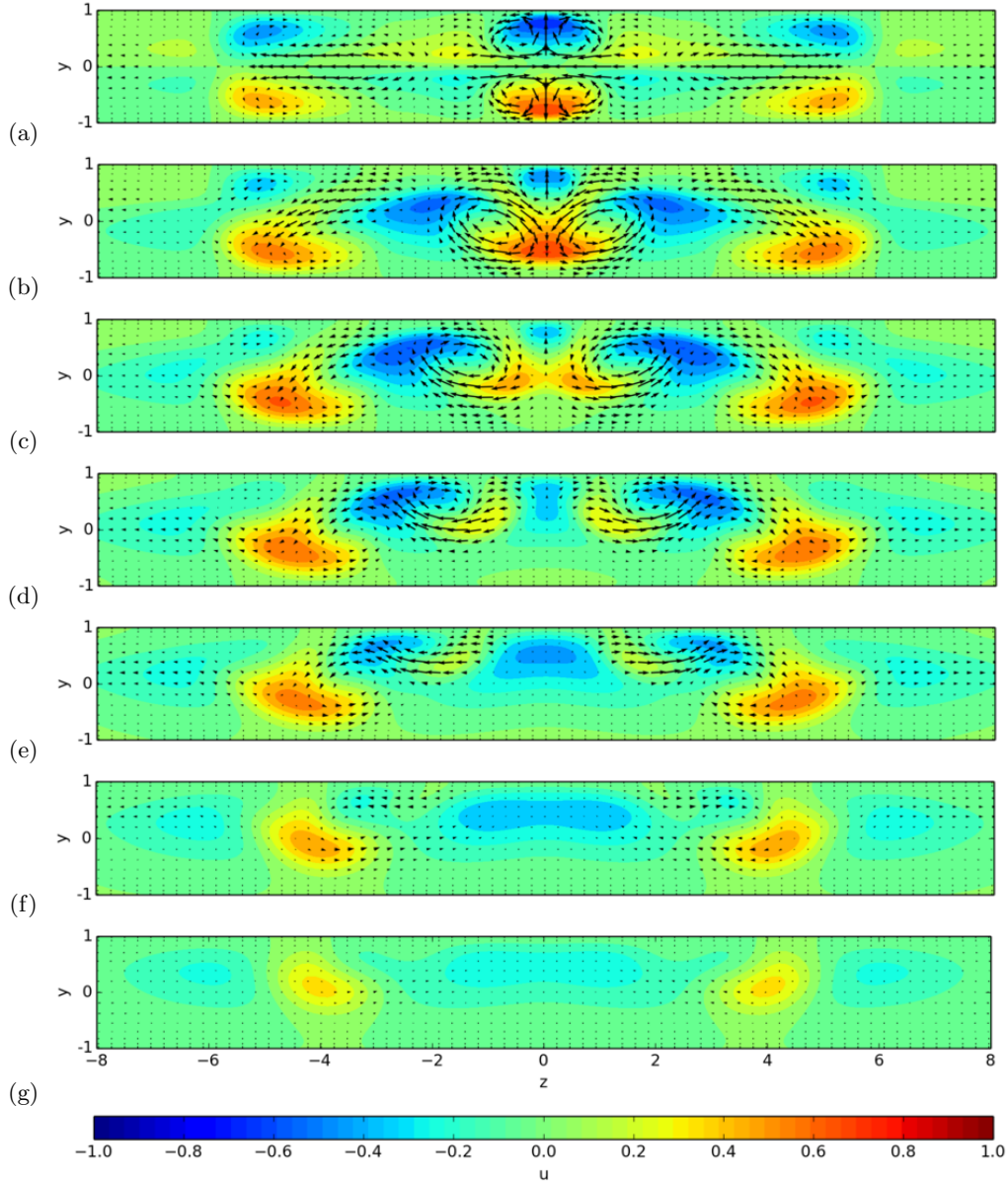


FIGURE 3. **Streamwise-normal cross sections of velocity.** Arrows indicate  $v, w$  velocity, and color indicates streamwise velocity  $u$ . The scaling of arrow length to  $v, w$  magnitude is the same in all graphs. (a-g) show  $y, z$  planes at  $x = \{0, 2.5, 5, 7.5, 10, 15, 20\}$ ; the positions of these planes are marked with dotted lines in figure 2.

strength. These are positioned at about  $z = \pm 3$ , and they span the distance between the walls. By  $x = 20$  in (g) swirling in both the legs and the flanking vortices has died out and all that remains are the streamwise streaks.

### 3.3. Exponential decay and overhang of the streamwise streaks

The long streamwise tails of the doubly-localized solution are dominated by a spanwise-localized band of streaky streamwise velocity. Here we provide a linear analysis that

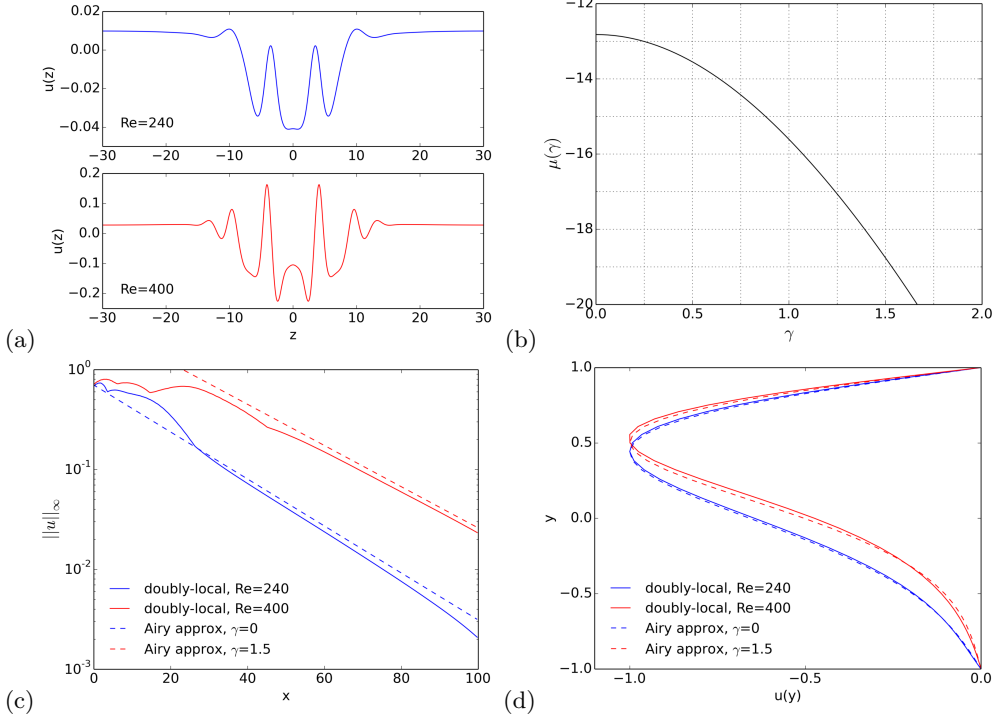


FIGURE 4. **Streamwise decay of streaks.** (a) The streamwise velocity  $u$  as a function of spanwise coordinate  $z$  at  $x = 50$  (within the streamwise tail) and at  $y = 0.5$  (near the peak of the overhang profile). (b) Coefficient  $\mu$  of exponential streamwise decay rate  $\exp(\mu x/Re)$  as a function of spanwise wavenumber  $\gamma$  for the Airy-function approximation of the tails. (c) Exponential decay of streamwise tails in the doubly-localized solution at  $Re = 240$  and  $400$  compared to the  $\exp(\mu(\gamma)x/Re)$  prediction.  $\|u\|_\infty$  denotes the maximum magnitude of  $u$  over  $(y, z)$  as a function of  $x$ . (d) Wall-normal overhang profile  $u(y)$  at  $x = 50$  and  $z = 0$ , compared to predicted  $\hat{u}(y)$  (all curves normalized to unit amplitude).

accounts for the exponential streamwise decay rate of the streamwise tails and the form of their wall-normal overhang profile, effects observed in turbulent spots by Lundbladh & Johansson (1991) and Duguet & Schlatter (2013). Direct numerical evaluation of the magnitudes of different terms in the  $u$  component of the Navier-Stokes equation (2.1) for the doubly-localized solution shows that the dominant terms in the streamwise tails are

$$yu_x = Re^{-1}(u_{yy} + u_{zz}) \quad (3.2)$$

where subscripts indicate differentiation. Although the solution is localized in  $z$ , a good approximation for the decay rate and overhang profile can be obtained by assuming a  $z$ -periodic solution of the form  $u(x, y, z) = \hat{u}(y) \exp(i\gamma z + \mu x/Re)$  with  $\gamma$  set to match the dominant spanwise wavenumber observed in the streaky tails. Substitution of this ansatz into (3.2) results in the ODE

$$\hat{u}''(y) - (\gamma^2 + \mu y) \hat{u}(y) = 0, \quad (3.3)$$

which has solutions

$$\hat{u}(y) = a \text{Ai}(\gamma^2 \mu^{-2/3} + \mu^{1/3} y) + b \text{Bi}(\gamma^2 \mu^{-2/3} + \mu^{1/3} y), \quad (3.4)$$

---

$Re$	$\langle \sigma_{xy}, \sigma_z \rangle$		$\langle \sigma_{xy}, -\sigma_z \rangle$		$\langle -\sigma_{xy}, \sigma_z \rangle$		$\langle -\sigma_{xy}, -\sigma_z \rangle$	
	pos. $\lambda_r$	max. $\lambda_r$	pos. $\lambda_r$	max. $\lambda_r$	pos. $\lambda_r$	max. $\lambda_r$	pos. $\lambda_r$	max. $\lambda_r$
240	2	0.0370	3	0.0414	3	0.0329	8	0.1283
300	4	0.0278	7	0.0314	5	0.0286	14	0.1028
340	6	0.0265	9	0.0635	7	0.0636	15	0.0952
360	8	0.0750	9	0.0751	7	0.0751	15	0.0920
380	8	0.0853	11	0.0854	12	0.0854	19	0.0892
400	17	0.0955	12	0.0958	16	0.0958	23	0.0960

---

TABLE 1. **Instabilities of the doubly-localized solution.** The number of unstable eigenfunctions (positive real part) and the real part of the most unstable eigenvalue are given for each eigenfunction symmetry group and a range of Reynolds numbers.

---

where Ai and Bi are Airy functions. The boundary conditions  $\hat{u}(\pm 1) = 0$  determine  $\mu$  and the relative values of  $a$  and  $b$  as a function of  $\gamma$ . Nontrivial solutions of (3.4) require

$$\text{Ai}(\gamma^2 \mu^{-2/3} + \mu^{1/3}) \text{Bi}(\gamma^2 \mu^{-2/3} - \mu^{1/3}) - \text{Ai}(\gamma^2 \mu^{-2/3} - \mu^{1/3}) \text{Bi}(\gamma^2 \mu^{-2/3} + \mu^{1/3}) = 0 \quad (3.5)$$

which we solve numerically for  $\mu$  as a function of  $\gamma$ , choosing the negative solution  $\mu(\gamma)$  closest to zero in order to find the solution with slowest streamwise decay.

Figure 4(b) shows  $\mu$  as a function of  $\gamma$ . The  $\gamma \approx 0$  modes have the slowest exponential decay, so as  $x \rightarrow \infty$  we expect the tails to be dominated by the  $\gamma = 0$  or fundamental  $\gamma = 2\pi/L_z$  mode. This behavior is evident for the doubly-localized equilibrium at  $Re = 240$ . Figure 4(a) shows that the streamwise velocity at  $x = 50$  has a wide slow streak in the region  $|z| < 10$  with weaker small-scale  $z$  variation. The power spectrum of this function has its strongest peak by nearly an order of magnitude at the fundamental wavenumber  $\gamma = 2\pi/L_z \approx 0.1$ . The decay rate  $\mu(\gamma)$  is nearly constant for small  $\gamma$ , so for  $Re = 240$  we take  $\gamma = 0$  and find  $\mu(0) \approx -13$ . Figure 4(c) shows good agreement between the predicted decay  $\exp(-13x/240)$  and that observed in the doubly-localized solution. Figure 4(d) shows good agreement between the predicted profile  $\hat{u}(y)$  from (3.4) and the streamwise velocity profile  $u(y)$  of the doubly-localized solution at  $x = 50, z = 0$ .

However, the  $1/Re$  factor in  $\exp(\mu x/Re)$  means that small  $z$ -wavelength transients of sufficient magnitude can persist and even dominate the tails for  $x \ll Re$ . Figure 4(a) shows that at  $x = 50$  the small-wavelength  $z$  variation for the  $Re = 400$  solution is much stronger than for  $Re = 240$ . The power spectrum of this  $z$  profile has peaks of nearly equal magnitude at the fundamental mode  $\gamma \approx 0.1$  and at  $\gamma \approx 1.5$ . From what follows we determine that the exponential decay in  $\|u\|_\infty$  for the  $z$ -localized structure is governed by the slightly less energetic  $\gamma \approx 1.5$  mode. Since  $\mu(1.5) \approx -19$  from figure 4(b), the decay of this mode is  $\exp(-19x/400)$ , which is only a factor of two smaller than the  $\exp(-13x/400)$  decay of the  $\gamma = 0$  mode over a length  $x \approx 50$ . The match of this decay rate in figure 4(c) and the corresponding overhang function in figure 4(d) to the doubly-localized solution confirms that at  $Re = 400$  the tails for  $x < 80$  are governed by the faster-decaying  $\gamma \approx 1.5$  mode. For  $x = O(Re)$  and larger, beyond the limits of the present computational domain, we expect the large- $\gamma$  transients to die out leaving the tails dominated by more slowly decaying small- $\gamma$  modes.

#### 3.4. Stability and the evolution of unstable perturbations

In minimal flow units, the transition to turbulence is governed by invariant ‘edge state’ solutions whose stable manifolds form separatrices between states that quickly decay towards laminar flow and states that become turbulent (Wang *et al.* 2007; Schneider



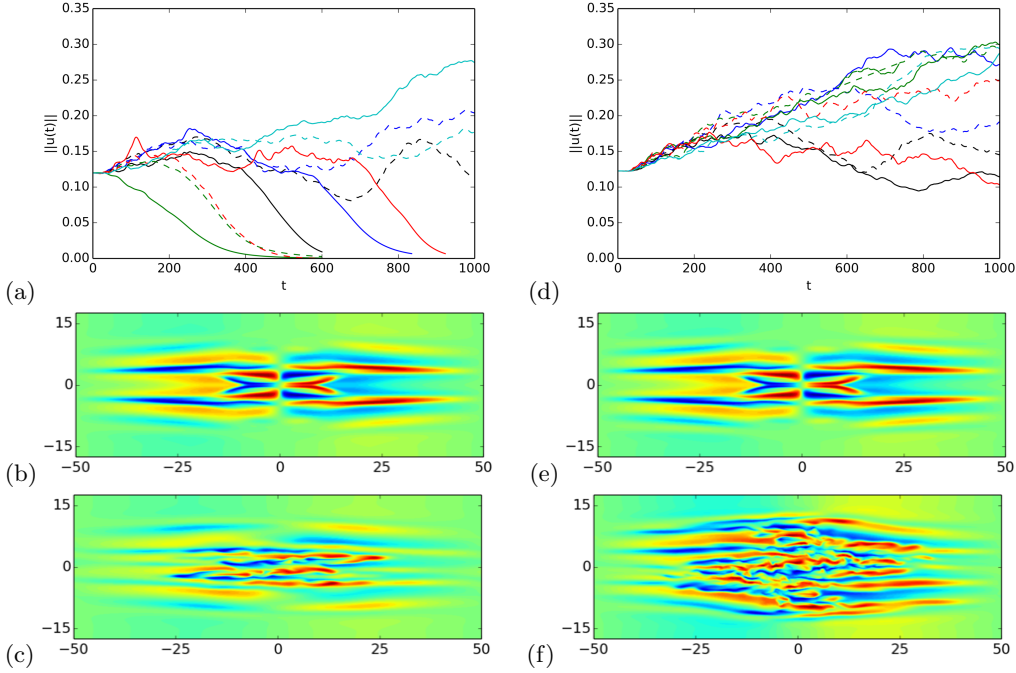


FIGURE 5. **Evolution of unstable eigenfunctions.** (a,d) show  $\|\mathbf{u}(t)\|$  versus time  $t$  for small perturbations of the doubly-localized solution along its most unstable eigenfunctions, at (a)  $Re = 380$  and (d)  $Re = 400$ . Color denotes the symmetries of the eigenfunction perturbations: red for  $\langle \sigma_{xy}, \sigma_z \rangle$  symmetric eigenfunctions, black for  $\langle \sigma_{xy}, -\sigma_z \rangle$ , blue for  $\langle -\sigma_{xy}, \sigma_z \rangle$ , green for  $\langle -\sigma_{xy}, -\sigma_z \rangle$ , and cyan for perturbations along combinations of eigenfunctions that break all symmetries. Solid lines indicate the most unstable eigenfunction of each symmetry group, and dashed are the second-most unstable. The midplane streamwise velocity of the most unstable perturbation at (b)  $t = 0$  and (c)  $t = 200$  for  $Re = 380$ , and (e,f) the same for  $Re = 400$ .

*et al.* 2008). Efforts to develop a similar dynamical understanding of transition in extended flows have lead to the computation of a number of localized edge states, but to date these have either been invariant states localized in a single homogeneous direction (Schneider *et al.* 2010b; Avila *et al.* 2013; Khapko *et al.* 2013; Zammert & Eckhardt 2014) or doubly-localized but chaotically wandering states without well-defined stable and unstable manifolds (Schneider *et al.* 2010b; Duguet *et al.* 2012). The doubly-localized invariant solution in this paper thus provides a potential starting point for addressing spatiotemporal transition of extended flows in dynamical terms. We focus on a  $100 \times 30$  domain, large enough to exhibit a range of spatiotemporal behavior (Philip & Manneville 2011), and  $230 \leq Re \leq 400$ , above the  $Re \approx 228$  saddle-node bifurcation point of the doubly-localized solution. Table 1 summarizes the properties of the leading unstable eigenfunctions categorized by symmetry group. The eigenfunctions  $\mathbf{v}$  of the linearized dynamics about the doubly-localized solution are either symmetric ( $\mathbf{v} = \sigma \mathbf{v}$ ) or antisymmetric ( $\mathbf{v} = -\sigma \mathbf{v}$ ) for each symmetry of the solution and thus have one of four symmetry groups:  $\langle \sigma_{xy}, \sigma_z \rangle$ ,  $\langle \sigma_{xy}, -\sigma_z \rangle$ ,  $\langle -\sigma_{xy}, \sigma_z \rangle$ , or  $\langle -\sigma_{xy}, -\sigma_z \rangle$ .

Figure 5 characterizes the temporal evolution  $\mathbf{u}(t) = f^t(\mathbf{u}_0 + \delta \mathbf{u})$  of the doubly-localized solution  $\mathbf{u}_0$  perturbed along its most unstable eigenfunctions and along combinations of eigenfunctions that break all symmetries. Perturbation magnitudes were set to  $\|\delta \mathbf{u}\|/\|\mathbf{u}_0\| = 10^{-2}$ , where  $\|\mathbf{u}\|^2 = 1/V \int_V \mathbf{u} \cdot \mathbf{u} \, dx$ , with  $V$  the volume of the compu-

tational domain. For  $Re \leq 360$  (not shown) most perturbations produce a short period ( $t < 200$ ) of transient growth, but in all cases monotonic relaminarization  $\|\mathbf{u}(t)\| \rightarrow 0$  begins by  $t \approx 500$ . At  $Re = 380$ , several perturbations produce long-lived ( $t > 1000$ ) turbulent spots, and at  $Re = 400$  all perturbations do. Figure 5(b,c) shows a typical decaying spot at  $Re = 380$ , and figure 5(e,f) shows a typical growing spot at  $Re = 400$ .

Unlike edge states, the doubly-localized solution has stable manifold of co-dimension greater than 1 for all Reynolds numbers (even with  $\langle \sigma_{xy}, \sigma_z \rangle$  symmetry restriction), so the stable manifold cannot divide state space and form a laminar/turbulent boundary by itself. However, the fact that some perturbations from the doubly-localized solution lead to laminar flow and some to turbulence demonstrates that the solution lies on the laminar/turbulent boundary, and that portions of its unstable eigenspace lie on either side of the boundary, for the approximate range  $360 \lesssim Re \lesssim 400$ . For  $Re \leq 360$ , the solution lies on the laminar side of the boundary, and  $Re \geq 400$ , it lies on the turbulent side. In all cases the perturbations rapidly generate fine-scale structure in the velocity field, which then either decays or grows in a complex, long-term, and perturbation- and Reynolds-dependent manner. Note that oblique perturbations (with  $\sigma_{xyz} \in \langle -\sigma_{xy}, -\sigma_z \rangle$  symmetry) produce turbulent spots with  $\sigma_{xyz}$  symmetry but little noticeable obliqueness (figure 5(c,f)), though eventually such spots can grow to fill the computational domain with a pattern of tilted laminar/turbulent bands.

#### 4. Conclusions

We have computed a doubly-localized solution of plane Couette flow, which consists of two symmetrically-opposed  $\Lambda$ -shaped vortices whose legs swirl in opposite directions and are tilted in both the spanwise and wall-normal directions. The solution roughly resembles in size and internal structure the smallest sustained turbulent spots simulated by Lundbladh & Johansson (1991) at similar Reynolds number and the doubly-localized, chaotically wandering edge states of Duguet *et al.* (2009) and Schneider *et al.* (2010b). The streamwise exponential decay and the form of the wall-normal overhang profile are well-approximated by the solution of a linearized equation involving the leading terms of the Navier-Stokes equations. Over a range of Reynolds numbers the solution lies on the boundary between states that decay to laminar flow and those that grow to turbulence.

**Acknowledgments.** The authors thank Tobias Schneider, Greg Chini, and Bruno Eckhardt for helpful discussions, Hecke Schrobendorff and Tobias Kreilos for their work on parallelizing `channelflow`, and the Max Planck Institute for Dynamics and Self-Organization for computer time.

#### REFERENCES

- AVILA, M, MELIBOVSKY, F, ROLAND, N & HOF, B 2013 Streamwise-localized solutions at the onset of turbulence in pipe flow. *Physical Review Letters* **110** (22), 224502.
- BARKLEY, D. & TUCKERMAN, L.S. 2005 Computational Study of Turbulent Laminar Patterns in Couette Flow. *Phys. Rev. Lett.* **94**, 014502.
- DEGUCHI, K., HALL, P. & WALTON, A. 2013 The emergence of localized vortex-wave interaction states in plane Couette flow. *J. Fluid Mech.* **721**, 58–85.
- DUGUET, Y. & SCHLATTER, P. 2013 Oblique laminar-turbulent interfaces in plane shear flows. *Phys. Rev. Lett.* **110**, 034502.
- DUGUET, Y., SCHLATTER, P. & HENNINGSON, D. 2009 Localized edge states in plane Couette flow. *Phys. Fluids* **21**, 111701.

- DUGUET, Y., SCHLATTER, P., HENNINGSON, D.S. & ECKHARDT, B. 2012 Self-sustained localized structures in a boundary-layer flow. *Phys. Rev. Lett.* **108**, 044501.
- GIBSON, J.F. 2014 Channelflow: a spectral Navier-Stokes simulator in C++. *Tech. Rep.*. Univ. New Hampshire, [www.channelflow.org](http://www.channelflow.org).
- GIBSON, J.F. & BRAND, E. 2014 Spanwise-localized solutions of planar shear flows. *J. Fluid Mech.* **745**, 25–61.
- GIBSON, J. F., HALCROW, J. & CVITANOVIĆ, P. 2008 Visualizing the geometry of state space in plane Couette flow. *J. Fluid Mech.* **611**, 107–130, [arXiv:0705.3957](https://arxiv.org/abs/0705.3957).
- GIBSON, J. F., HALCROW, J. & CVITANOVIĆ, P. 2009 Equilibrium and traveling-wave solutions of plane Couette flow. *J. Fluid Mech.* **638**, 1–24, [arXiv:0808.3375](https://arxiv.org/abs/0808.3375).
- HOF, B., WESTERWEEL, J., SCHNEIDER, T.M. & ECKHARDT, B. 2006 Finite lifetime of turbulence in shear flows. *Nature* **443** (7107), 59–62.
- ITANO, T. & GENERALIS, S. C. 2009 Hairpin vortex solution in planar Couette flow: A tapestry of knotted vortices. *Phys. Rev. Lett.* **102**, 114501.
- KAWAHARA, G., UHLMANN, M. & VAN VEEN, L. 2012 The significance of simple invariant solutions in turbulent flows. *Ann. Rev. Fluid Mech.* **44**, 203–225.
- KHAPKO, T., KREILOS, T., SCHLATTER, P., DUGUET, Y., ECKHARDT, B. & HENNINGSON, D. 2013 Localized edge states in the asymptotic suction boundary layer. *J. Fluid Mech.* **717**, R6.
- LUNDBLADH, A. & JOHANSSON, A. V. 1991 Direct simulation of turbulent spots in plane Couette flow. *J. Fluid Mech.* **229**, 499–516.
- NAGATA, M. 1990 Three-dimensional finite-amplitude solutions in plane Couette flow: bifurcation from infinity. *J. Fluid Mech.* **217**, 519–527.
- PHILIP, J. & MANNEVILLE, P. 2011 From temporal to spatiotemporal dynamics in transitional plane Couette flow. *Phys. Rev. E* **83**, 036308.
- SCHNEIDER, T.M., GIBSON, J.F., LAGHA, M., LILLO, F. DE & ECKHARDT, B. 2008 Laminar-turbulent boundary in plane Couette flow. *Phys. Rev. E* **78**, 037301.
- SCHNEIDER, T. M., GIBSON, J. F. & BURKE, J. 2010a Snakes and ladders: Localized solutions of plane Couette flow. *Phys. Rev. Lett.* **104**, 104501.
- SCHNEIDER, T. M., MARINC, D. & ECKHARDT, B. 2010b Localized edge states nucleate turbulence in extended plane Couette cells. *J. Fluid Mech.* **646**, 441–451.
- SCHUMACHER, J. & ECKHARDT, B. 2001 Evolution of turbulent spots in a parallel shear flow. *Phys. Rev. E* **63**, 046307.
- TILLMARK, N. & ALFREDSSON, P. H. 1992 Experiments on transition in plane Couette flow. *J. Fluid Mech.* **235**, 89–102.
- VISWANATH, D. 2007 Recurrent motions within plane Couette turbulence. *J. Fluid Mech.* **580**, 339–358.
- VISWANATH, D. 2009 The critical layer in pipe flow at high Reynolds number. *Phil. Trans. R. Soc. A* **367**, 561–576.
- WANG, J., GIBSON, J.F. & WALEFFE, F. 2007 Lower branch coherent states in shear flows: Transition and control. *Phys. Rev. Lett.* **98** (20), 204501.
- WU, Y. & CHRISTENSEN, K.T. 2006 Population trends of spanwise vortices in wall turbulence. *J. Fluid Mech.* **568** (1), 55–76.
- WYGNANSKI, I. J. & CHAMPAGNE, F. H. 1973 On transition in a pipe. Part 1: The origin of puffs and slugs and the flow in a turbulent slug. *J. Fluid Mech.* **59**, 281–335.
- ZAMMERT, S. & ECKHARDT, B. 2014 Periodically bursting edge states in plane Poiseuille flow. [arXiv:1312.6783v2](https://arxiv.org/abs/1312.6783v2).
- ZHOU, J., ADRIAN, R.J., BALACHANDAR, S. & KENDALL, T.M. 1999 Mechanisms for generating coherent packets of hairpin vortices in channel flow. *J. Fluid Mech.* **387**, 353–396.